

Effects of potassium on kesterite solar cells: Similarities, differences and synergies with sodium

S. G. Haass,^{1,a} C. Andres,¹ R. Figi,² C. Schreiner,² M. Bürki,² A. N. Tiwari,¹ and Y. E. Romanyuk¹

¹Laboratory for Thin Films and Photovoltaics, Empa–Swiss Federal Laboratories for Materials Science and Technology, Ueberlandstrasse 129, 8600 Dübendorf, Switzerland

²Laboratory for Advanced Analytical Technologies, Empa–Swiss Federal Laboratories for Materials Science and Technology, Ueberlandstrasse 129, 8600 Dübendorf, Switzerland

(Received 10 November 2017; accepted 12 January 2018; published online 30 January 2018)

Addition of alkali dopants is essential for achieving high-efficiency conversion efficiency of thin film solar cells based on chalcogenide semiconductors like Cu(In,Ga)Se₂ (CIGS) and Cu₂ZnSn(S,Se)₄ (CZTSSe also called kesterite). Whereas the treatment with potassium allows boosting the performance of CIGS solar cells as compared to the conventional sodium doping, it is debated if similar effects can be expected for kesterite solar cells. Here the influence of potassium is investigated by introducing the dopant during the solution processing of kesterite absorbers. It is confirmed that the presence of potassium leads to an enhanced grain growth and a ten-fold lower potassium concentration is sufficient for obtaining grain size similar to sodium-containing absorbers. Potassium is located predominantly at grain boundaries and it suppresses incorporation of sodium into the absorber layer. The potassium doping increases the apparent carrier concentration to $\sim 2 \times 10^{16} \text{ cm}^{-3}$ for a potassium concentration of 0.2 at%. The potassium-doped solar cells yield conversion efficiency close to 10%, on par with only sodium-doped samples. Co-doping with potassium and sodium has not revealed any beneficial synergetic effects and it is concluded that both dopants exhibit similar effects on the kesterite solar cell performance. © 2018 Author(s). All article content, except where otherwise noted, is licensed under a Creative Commons Attribution (CC BY) license (<http://creativecommons.org/licenses/by/4.0/>). <https://doi.org/10.1063/1.5013114>

I. INTRODUCTION

Kesterite solar cells achieved up to 12.6 % conversion efficiency¹ but still suffer under a pronounced reduction of the open circuit voltage (V_{OC}), often expressed as V_{OC} – deficit, which is defined as $V_{OC} - \text{deficit} = E_g/q - V_{OC}$ with E_g the bandgap and q the elementary electric charge. Alkali doping of the kesterite absorber layer is a promising approach to tackle the high V_{OC} -deficit, but so far only in the case of sodium thorough investigations were conducted, revealing grain size enhancement, passivation of grain boundaries and an increase in net hole concentration.^{2–4} Potassium post deposition treatment (KF-PDT) resulted in a tremendous improvement for the related Cu(In,Ga)(S,Se)₂ (CIGS) solar cells,⁵ however similar results for a KF-PDT in kesterite solar cells could not be reproduced.⁶ Concerning potassium doping, first theoretical studies showed that potassium will be incorporated mostly as a substitutional defect for copper. The formation energy for K_{Cu} is higher compared to Na_{Cu} due to the larger size of potassium and therefore it is suggested that potassium is unlikely to replace sodium.⁷ Theoretical calculations and APT measurements show that potassium is predominantly located in grain boundary and interfaces.^{8–10} Experiments revealed that compared to sodium already ten-fold lower concentration of potassium results in a similar increase in grain size.¹¹ Potassium addition can enhance the 112 preferred orientation and reduce ZnS secondary phases in

^aCorresponding author, stefan.haass@empa.ch

solution processed CZTS absorber layers.¹² For solar cell devices, a reduction in the series resistance was observed upon potassium addition¹² whereas the carrier concentration could be increased for potassium as compared to sodium, rubidium, cesium or undoped samples.^{9,13}

In this study we investigate the impact of potassium addition on the kesterite absorber morphology, composition, lattice structure and the photovoltaic parameters of resulting kesterite solar cells. This approach exploits the advantage of solution processing which enables a controlled and homogeneous incorporation of alkali elements in to the precursor layer. Potassium was added to the precursor solution in various concentrations in the form of KCl which has a high solubility in the precursor solution. The subsequent process steps were conducted equally for all samples. It has to be pointed out that for these samples no sodium was added and a barrier layer of SiO_x between the soda-lime glass and Mo back contact was used to inhibit the diffusion of sodium from the SLG substrate. Nevertheless, due to the long annealing times at high temperatures sodium was still present in the absorber layer due to possible transport through the gas phase.¹⁴ Finally, in order to explore any synergetic effects between potassium and sodium, controlled amounts of KCl were added on top of a constant amount NaCl, and results are compared to the samples with only KCl addition.

II. EXPERIMENTAL DETAILS

The CZTSSe precursor solution consisted of thiourea (99%+, Sigma-Aldrich), SnCl₂·2H₂O (98%, Sigma-Aldrich), ZnCl₂ (99.99%, Alfa Aesar), CuCl₂ (98%+, Alfa Aesar), KCl (99.999%, Alfa Aesar) and NaCl (99.99%, Alfa Aesar), dissolved in Dimethyl sulfoxide (DMSO) (99.9%, Alfa Aesar). The precursor solution contained 0 – 100 mM KCl and for the second sample series 100 mM NaCl. A 200 – 300 nm thick SiO_x layer was sputtered onto a 1 mm thick soda-lime glass with a subsequent deposition of 1 μm of molybdenum. The precursor solution was spin-coated onto the Mo layer and dried on a hotplate at 320 °C in air. The spin-coating and drying steps were repeated 12 times in order to obtain the desired precursor film thickness of 1.5 – 2 μm. All samples were annealed in an Annealsys AS ONE 150 RTP furnace inside a closed graphite box with additional selenium pellets (800 mg). The temperature gradient employed for annealing was the 3-stage process with holding temperatures at 300 °C, 500 °C and 550 °C. After selenization the absorbers were immersed for 30 s in a 10 wt% KCN solution in order to clean the surface from contaminations and oxides. A 50-70 nm thick CdS buffer layer was deposited by chemical bath deposition, and a 70 nm/250 nm i-ZnO/Al:ZnO bi-layer was sputtered. A Ni/Al top grid and an AR coating of MgF₂ were deposited by e-beam evaporation. Individual solar cells were mechanically scribed with an area of $0.30 \pm 0.02 \text{ cm}^2$.

Metal ratios were measured by inductively coupled plasma mass spectrometry (ICP-MS), for which approximately 1 cm² of the kesterite solar cells were etched for 60 s in 5 wt% acetic acid solution in order to remove the window layer. Then kesterite absorber material was detached from the thin-film solar cell at the Mo/CZTSSe interface, directly transferred into 50 mL trace metal-free polyethylene tubes and fully dissolved in a mixture of 2.5 mL H₂O₂ 30% MERCK suprapure, 4 mL HNO₃ 67% MERCK ultrapure, and 2.5 mL HCl 32% MERCK ultrapure. After filling to 25 mL with 18 MΩcm de-ionized water, the sample was diluted 1:10 with 18 MΩcm de-ionized water for analysis. Metal determinations were performed on an Agilent 8800 triple quadrupole ICP-MS with different reaction modes such as He and O₂ and external calibration using certified metal standards (1000 μg mL⁻¹, Alfa Aesar Specpure). For quality assurance, analysis of reference materials and spiking experiments were performed, with recoveries between 90 and 110%.

All absorber layers were characterized by X-ray fluorescence (XRF), X-ray diffraction (XRD), secondary electron microscopy (SEM), time-of-flight secondary-ion-mass-spectrometry (ToF-SIMS) for structural and compositional characterization. SEM measurements were performed on a Hitachi S-4800 electron microscope using 20 kV acceleration voltage which results in an interaction volume of >1 μm. Cross section images were taken from mechanically cleaved samples. SIMS is used for depth profiles of complete solar cell stacks as well as imaging to reveal the lateral distribution of trace alkali metals. The measurements were recorded on a ToF-SIMS system from ION-TOF using O₂⁺ primary ions with 2 keV of ion energy, a current of 400 nA, and a raster size of 400 x 400 μm². An area of 100 x 100 μm² in the case of depth profiles and 20 x 20 μm² for the imaging mode was

analyzed using Bi^+ ions with 25 keV of ion energy. XRD patterns were recorded in $2\theta \setminus \theta$ scan mode using a Bruker D8 diffractometer with $\text{CuK}\alpha$ radiation ($\lambda = 1.5418 \text{ \AA}$, beam voltage: 40kV, beam current: 40 mA, calibrated using Si100 and Si111 single crystals), a step size of 0.04° and a scan rate of 0.5 s/step for the full pattern and a step size of 0.004° and a scan rate of 2s/step for the detailed pattern.

The J - V characterization of solar cell devices was performed under standard test conditions (100 mWcm^{-2} , 25°C , AM1.5G) using a solar simulator calibrated with a certified Si diode. The external quantum efficiency (EQE) spectra were recorded using a chopped white light source (900 W halogen lamp) with a LOT MSH-300 monochromator, which was calibrated with certified Si and Ge diodes. The illuminated area on the sample was 0.1 cm^2 including grid lines. C- V measurements were carried out with a LCR-meter from Agilent (E4990A) with an AC-voltage of 30 mV at room temperature. For T- JV measurements the solar cells are placed on a temperature controlled copper stage inside an evacuated cryostat cooled with liquid nitrogen and illuminated by a 100 W halogen lamp. The intensity of the incident light can be varied by two orders of magnitude from approximately $1 - 142 \text{ mWcm}^{-2}$ using neutral density filters. From illumination and temperature dependent J - V measurements the reversed saturation current J_0 and the ideality factor A were calculated. Reflectance measurements were conducted with a Shimadzu UV-3600 UV-Vis spectrophotometer with an integrating sphere and performed against a BaSO_4 or Spectralon (SRS-99-010, AS-01160-060) reference.

III. RESULTS AND DISCUSSION

The nominal concentrations of KCl added to the precursor solutions are 0, 1, 5, 10, 50 and 100 mM, which correspond to $\text{K}/(\text{Cu}+\text{Zn}+\text{Sn})$ ratios in percent of 0, 0.07 %, 0.35 %, 0.7 %, 3.5 % and 7 %. For simplicity the samples are denoted with molarity values throughout the article even though it is worth stressing that actual alkali concentrations inside kesterite absorbers measured by ICP-MS are significantly lower than nominal and do not exceed 0.2 at%.

A. Morphology, structure and composition

Fig. 1 shows the SEM cross section images of full devices with different amounts of KCl. For 0, 1 and 5 mM KCl the absorber layer exhibits a distinct bi-layer structure, which vanishes for KCl concentrations of $\geq 10 \text{ mM}$ and the grain size increases to up to $1 - 2 \text{ }\mu\text{m}$. We suggest a similar mechanism for a potassium assisted grain growth improvement as was suggest earlier for sodium:¹⁵ Chemisorption of gaseous Se during the high temperature selenization step leads to the formation of

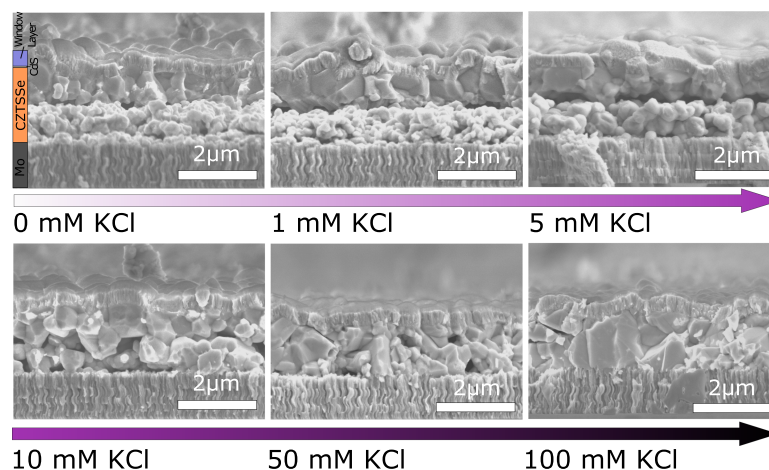


FIG. 1. SEM cross section images of full devices with increasing KCl concentration (no sodium addition). The morphology of the CZTSSe absorber layers exhibits a distinct bi-layer structure for 0 – 5 mM KCl. For $\geq 10 \text{ mM}$ KCl amount the grain size in the lower part of the absorber is increasing, yielding grains that span over the whole absorber layer thickness.

TABLE I. Metal ratios of the absorber layers with varying amounts of potassium measured by ICP-MS.

Sample	Cu/Sn	Cu/Zn	Cu/(Zn+Sn)	Zn/Sn
None	1.84	1.42	0.80	1.30
1 mM KCl	1.87	1.44	0.81	1.30
10 mM KCl	1.82	1.37	0.78	1.32
100 mM KCl	1.76	1.32	0.75	1.34

liquid potassium-polyselenide phases. These liquid phases act as a fluxing agent, thereby promoting selenium transport into the precursor layer and enhancing diffusion processes of less mobile phases during crystallization, resulting in increased grain size and overall improved morphology of the absorber layer.¹⁶

The formation of a $\text{Mo}(\text{S},\text{Se})_2$ layer during the high temperature annealing in chalcogen atmosphere can be estimated from the increase in the $\text{Mo}/\text{Mo}(\text{S},\text{Se})_2$ layer thickness and the appearance of the characteristic XRD Bragg reflexes. From SEM cross sections and overall back contact layer thickness a $\text{Mo}(\text{S},\text{Se})_2$ thickness of 200 – 300 nm is deduced, which is not affected by different KCl concentrations. The absorber layer thickness decreases with increasing KCl concentration due to the denser morphology of the absorber layer.

The precursor solution composition for all samples is identical – apart from the KCl concentration. Compositional measurements in Table I of copper (Cu), zinc (Zn) and tin (Sn) by ICP-MS show a lower copper content for 100 mM KCl compared to the lower concentration, which could be attributed to a reduced loss of tin and zinc during the high temperature annealing. The relatively lower copper content of the 100 mM KCl sample affects the bandgap and order/disorder of the Cu/Zn sublattice and will be discussed later.

In order to investigate the depth distribution inside the absorber layer potassium and sodium, SIMS measurements were performed. Traces of sodium stem from the SLG substrate, transported via the gas phase during the high-temperature annealing step.¹⁴ Additionally, minor diffusion of sodium

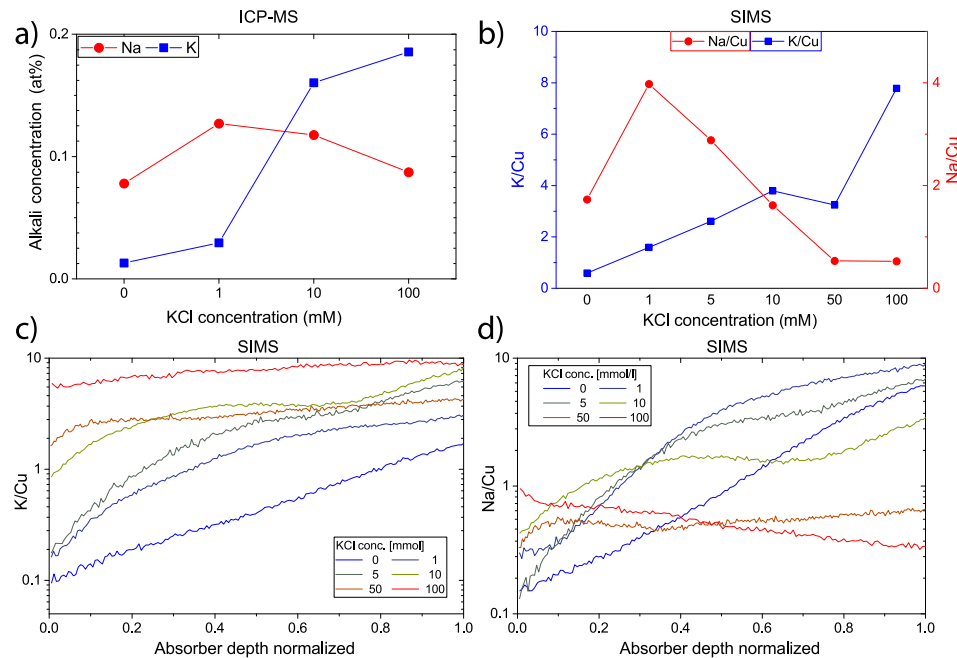


FIG. 2. a) Sodium and potassium content measured by ICP-MS. b) K/Cu and Na/Cu counts from SIMS measurements integrated over the whole absorber layer. ICP-MS and SIMS measurements exhibit similar results. In c) and d) the distribution of potassium and sodium inside the absorber layer is shown. The CdS/CZTSSe interface is located at the normalized absorber depth of 0 and the CZTSSe/ $\text{Mo}(\text{S},\text{Se})_2$ interface at 1.

through the SiO_x blocking layer cannot be ruled out. Fig. 2a) and b) show the relative amounts of potassium and sodium (the samples with 5 and 50 mM KCl were not measured by ICP-MS). Both measurement techniques reveal qualitatively the same results. For the SIMS measurements the integrated sodium and potassium counts were divided by the integrated copper counts inside the absorber layer. Copper is chosen as the reference element because the copper amount is constant throughout the absorber depth and exhibits similar quantities in all samples. A higher nominal KCl concentration leads to an increase in the measured potassium amount, which demonstrates the successful incorporation of potassium into the absorber layer by simply adding KCl to the precursor solution. While for the quantity of 1 mM KCl 85% of the nominal KCl content in the precursor solution is still present in the final absorber layer, for 10 mM 45 % and for 100 mM 4 % are still present in the final layer. How potassium is lost during the solar cell synthesis was not further investigated in this study.

Interestingly, the amount of sodium is first increasing followed by a decrease with subsequently increased KCl concentrations. The reduction of sodium concentration upon addition of potassium was also observed in highly efficient CIGS thin film solar cells.^{5,17} The distribution of both alkali elements is depicted in Fig. 2c), d) and reveals that for the samples with a distinct bi-layer structure the alkali metal concentrations are increased in the small-grained, lower part of the absorber layer. The profile flattens for the samples with large grains and no bi-layer structure (≥ 10 mM). The signal increase in the front of the absorber layer from 0 to 100 mM KCl for both potassium and sodium suggests that the alkali elements accumulate predominantly at the grain boundaries. An accumulation of potassium at the front interface between the buffer and absorber layer reported by Li et al.⁹ cannot be confirmed by this study. Alloying of potassium within the kesterite lattice is unlikely due to the large size of 1.66 Å of the potassium ion and thus high migration and substitution energies of ≥ 0.3 eV and 1.53 eV, respectively.⁸ Previous studies about the localization of potassium in chalcogenide absorber layers by APT revealed that potassium is segregating at the grain boundaries^{10,18} and SIMS imaging on the sample with 100 mM KCl concentration also indicates segregation of potassium (see Fig. 1 of the supplementary material).

Fig. 3a) shows the XRD patterns of the full devices including CdS, i-ZnO/Al:ZnO, Ni/Al grid and MgF_2 . All samples produce equivalent kesterite specific Bragg reflexes at 14.7° , 17.4° and 22.1° . For the sample with 100 mM KCl a $\text{Sn}(\text{S},\text{Se})_2$ Bragg reflex at 14.07° can be observed.¹⁹ The FWHM of the main 112 Bragg reflex in Fig. 3b) is lower for samples with ≥ 10 mM KCl concentration, suggesting an increase in grain size and crystal quality which is in agreement with the SEM cross section images in Fig. 1.

B. Opto-electronic properties

The internal quantum efficiency (IQE) patterns of the samples are presented in Fig. 4 and were calculated using the reflectance measured on the whole device including metal grid lines with $\text{IQE}(\lambda) = \text{EQE}(\lambda)/(1-R(\lambda))$. The bandgap determined by the inflection points in the long-wavelength

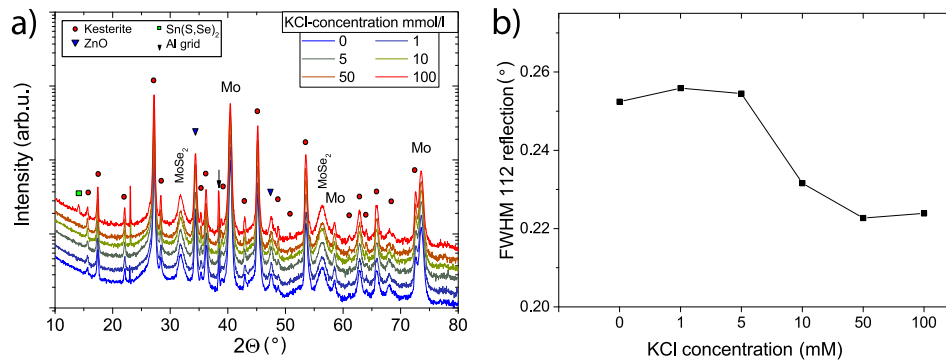


FIG. 3. a) XRD patterns of the full devices including CdS, i-ZnO/Al:ZnO, MgF_2 and Ni/Al grid. The FWHM of the main 112 Bragg reflex is presented in b).

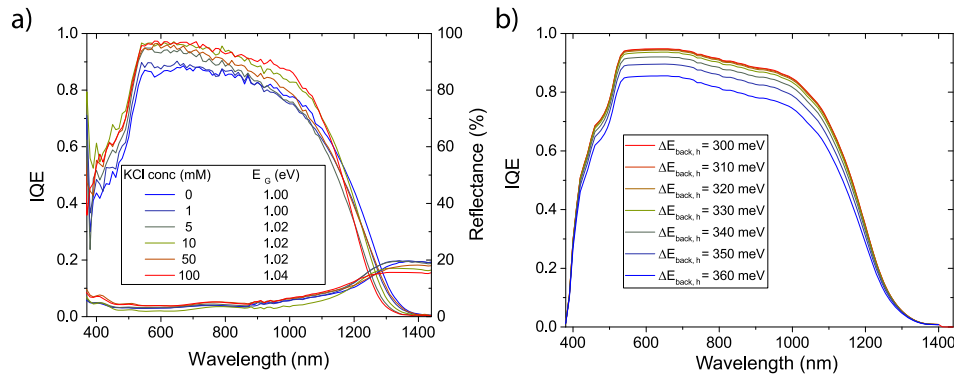


FIG. 4. a) IQE of all samples calculated from EQE and reflectance measurements. b) Results of SCAPS simulations including a back barrier with a height between 0.30 eV – 0.36 eV, which can reproduce the observed IQE behavior in a).

region increases from 1.00 eV for 0 mM KCl up to 1.04 eV for 100 mM KCl. The bandgap increase is connected to the decrease in Cu/(Zn+Sn) ratio leading to an increase in ordering of the Cu/Zn sublattice, which leads to a higher bandgap.²⁰ Detailed measurements of the 400/008 Bragg reflexes in Fig. 2 of the [supplementary material](#) were conducted, but due to the change in FWHM of the XRD Bragg peaks, a deconvolution to extract the tetragonal distortion and confirm the increase in ordering was not possible.

The shape of the IQE curves in the long wavelength region does not indicate a strong change in the collection efficiency with increasing KCl concentration. This implies an almost constant space charge region (SCR) width, which is in agreement with room-temperature C-V measurements in Fig. 5, which reveal only a slight increase in the apparent carrier concentration. A significant decrease of the apparent carrier concentration was measured with decreasing relative copper content.²¹ Therefore, the slight increase in apparent carrier concentration in combination with the decrease in relative copper content for this sample series indicates that potassium doping increases the carrier concentration. This result is in agreement with reported effects of potassium doping in kesterite solar cells by Li et al. and Hsieh et al.^{9,13}

The IQE value is rising from 0.85 to 0.97 in the wavelength range from 550 – 700 nm and could be explained by a removal of a barrier between the absorber layer and back contact for holes towards the back contact. SCAPS simulations²² with a barrier height between 0.30 eV– 0.36 eV can reproduce the observed IQE behavior (Fig. 4b).²³ In the simulations the focus was solely to investigate the increase in the IQE and the increase in bandgap was therefore not simulated.

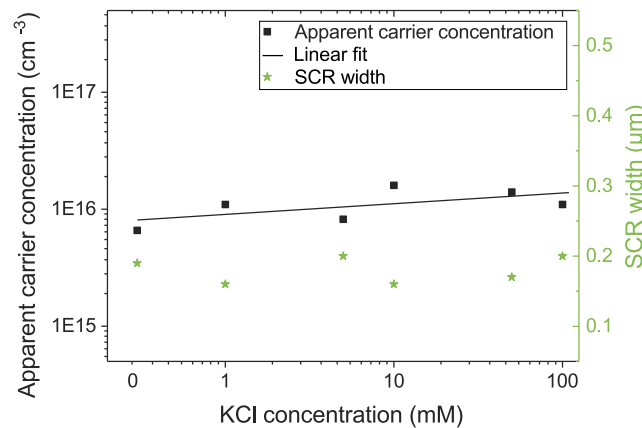


FIG. 5. Apparent carrier concentrations and SCR widths for samples prepared with 0 – 100 mM KCl concentration, derived from room temperature C-V measurements.

The increase of the IQE value could also stem from other effects, e.g. a spike in the conduction band alignment of the kesterite absorber and CdS buffer layer. However, due to the high series resistance that is reduced and the bi-layer structure that is transformed into a well crystallized absorber layer for ≥ 10 mM KCl concentrations, a hole barrier stemming from the small grained layer in the vicinity of the back contact offers the best explanation for the overall lower EQE and higher series resistance.

C. PV properties

Fig. 6 and Fig. 7 exhibit the photovoltaic parameters for all 6 samples with different KCl concentrations. Each sample consists of 9 cells, represented by box plots, with a cell size of $0.30 \pm 0.02 \text{ cm}^2$. The series resistance in a) is reduced with increased KCl concentrations, which is in agreement with the improved crystallization of the absorber layer in the vicinity of the back contact. The parallel resistance is constant for lower and decreases rapidly for 50 and 100 mM KCl concentrations. The shunting behavior coincides with the appearance of $\text{Sn}(\text{S},\text{Se})_2$ secondary phase identified by XRD and shown in Fig. 3. The ideality factor A is rising for increasing KCl concentrations and J_0 shows a minimum value for the 10 mM sample, indicating that undesirable recombination is lowest in this sample. From these parameters it can be assumed that 10 mM KCl is the optimal concentration due to reduced series resistance, improved morphology and lowest J_0 but without the formation of secondary phases that deteriorate the device performance.

Fig. 7 shows the best device with 9.7 %, 432 mV V_{OC} , 61 % FF and 36.7 mAcm^{-2} for 10 mM KCl. Taking the increase in bandgap into account, the V_{OC} - deficit remains constant around 0.62 – 0.64 V for all samples with the exception of the sample with 10 mM KCl concentration, which exhibits the lowest V_{OC} - deficit of 0.59 V. The higher J_{SC} value of the 10 mM KCl sample is partly due to an overall lower reflectance of the sample as shown in Fig. 4a).

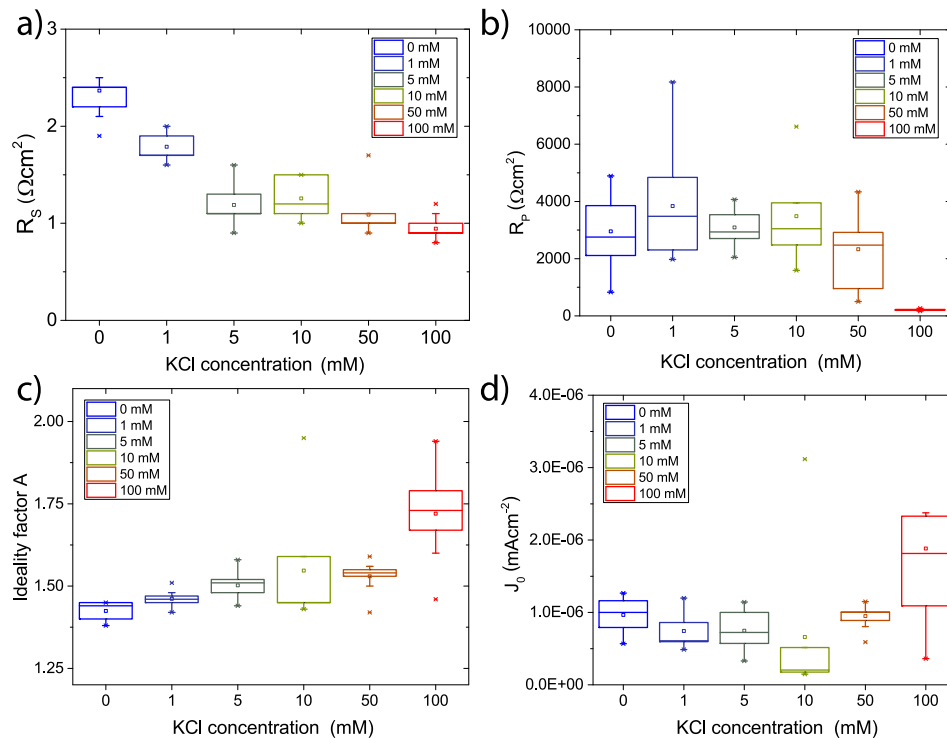


FIG. 6. a) The series resistance decreases with increasing KCl amount. b) The parallel resistance is decreasing from nominal 50 mM KCl onwards. c) The ideality factor A rises with increasing KCl content. d) The reversed saturation current J_0 shows a minimum for 10 mM and increases for 50 and 100 mM KCl concentrations.

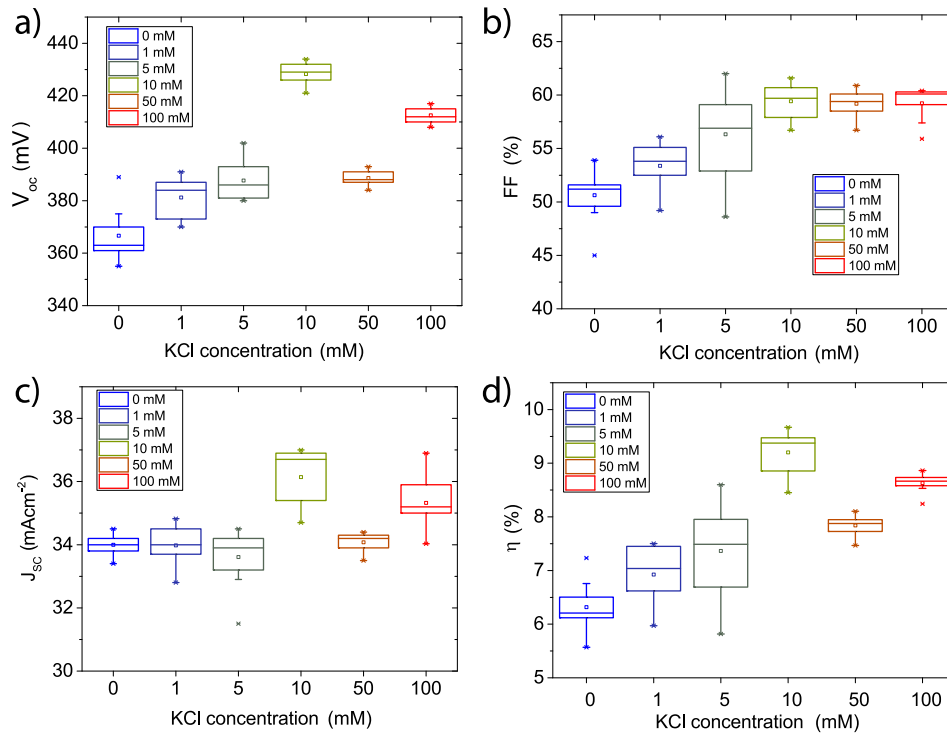


FIG. 7. a) – d) PV parameters with increasing KCl content yielding efficiencies of up to 9.7 % for 10 mM KCl. Experiments with different metal ratios²¹ and alkali elements reveal that 10 mM is the optimal concentration for the metal ratios used for this study, because of $\text{Sn}(\text{S},\text{Se})_2$ formation at higher than 10 mM KCl concentration.

The improvement of the FF can be attributed predominantly to the reduction of the series resistance R_s (Fig. 6a). It should be noted that the comparably high performance of the sample with 100 mM KCl is surprising when taking the low parallel resistance, high J_0 and the appearance of $\text{Sn}(\text{S},\text{Se})_2$ secondary phase into account. However, experiments with different metal ratios and alkali elements revealed that indeed 10 mM is the optimal concentration for the metal ratios used for this study, and with higher than 10 mM KCl concentration formation of $\text{Sn}(\text{S},\text{Se})_2$ deteriorates the device performance.²¹

D. Comparison to sodium doping

In order to reveal if addition of potassium to CZTSSe exhibits any additional effects on sodium-containing samples, a series of samples with different amount of KCl (0 – 100 mM KCl) and 100 mM NaCl was studied. Kesterite solar cells grown with 100 mM NaCl added to the precursor solution are described elsewhere.²⁴ The morphology of the samples with 100 mM NaCl and different KCl concentrations are shown in the SEM cross sections in Fig. 8, and they exhibit that NaCl is less effective in promoting grain growth compared to KCl. This can be due to the lower melting point of K_xSe phases (160 °C) as compared to Na_xSe phases (255 °C),^{16,25} which both act as a fluxing agent and improve the grain growth.^{11,15}

Fig. 9a) and b) show the device performance and V_{OC} - deficit for added KCl concentrations varying from 0 to 100 mM. From 0 to 50 mM KCl both efficiency and V_{OC} - deficit show a similar trend with average efficiencies of >9 % and V_{OC} - deficits below 0.6 V. For the 100 mM KCl sample a drop in efficiency below 6 % and a high V_{OC} - deficit of 0.7 V are observed and correlated to the appearance of $\text{Sn}(\text{S},\text{Se})_2$ secondary phase with the associated decrease in parallel resistance and V_{OC} , similar to the sample with only 50 or 100 mM KCl.

The IQE patterns of the 100 mM NaCl samples with different KCl amounts are shown in Fig. 9c). In contrast to the sample series without NaCl no reduction of the IQE value in the wavelength range of 550 - 700 nm can be observed here, suggesting that the presence of sodium lowers or removes

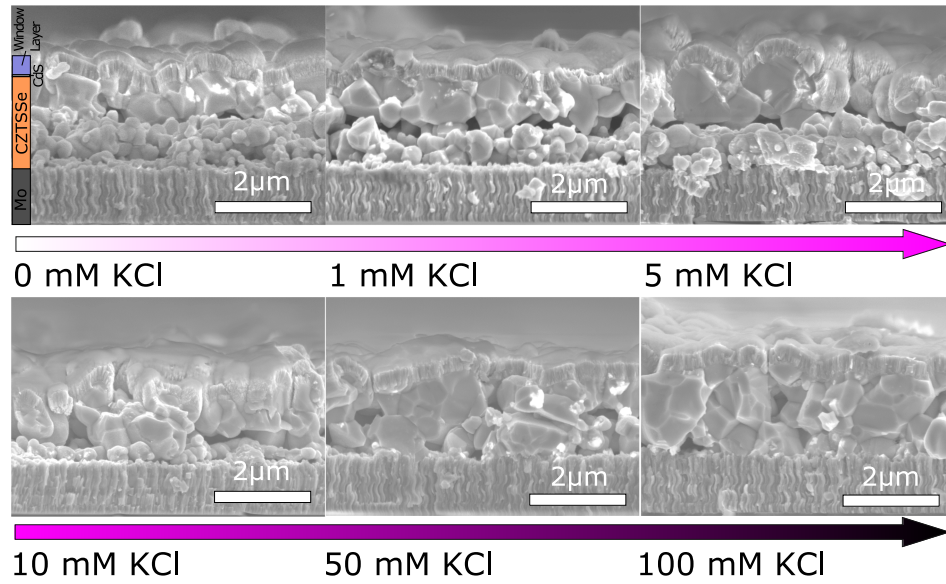


FIG. 8. SEM cross section images of the full devices including the window layer. The added KCl amount is increasing from 0 – 100 mM while the NaCl concentration remains at 100 mM for all samples.

the back barrier by either improving the morphology of the lower part of the absorber layer or increasing the hole conductivity of the back interface and grain boundaries. The decrease in the collection in the long-wavelength region for the sample with 100 mM KCl concentration is connected to the reduced V_{OC} and therefore assumed lower minority carrier lifetime. The reason for the similarly low collection in the long-wavelength region for the 50 mM KCl sample is unclear.

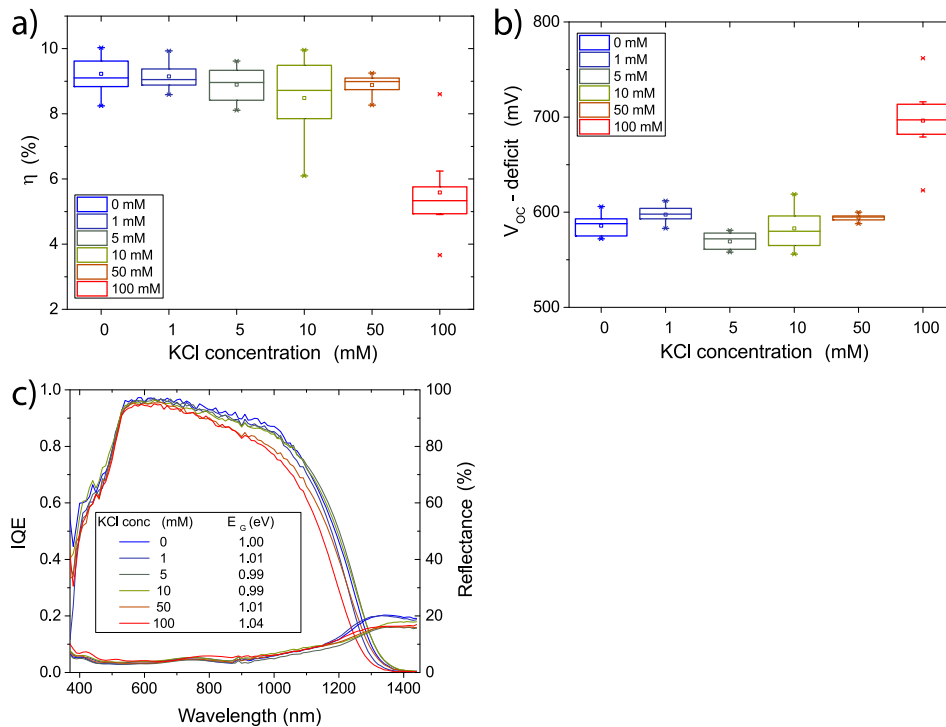


FIG. 9. a) – c) The PV parameters and IQE spectra of samples with 100 mM NaCl and 0 – 100 mM KCl.

TABLE II. Comparison of PV parameters for the best samples with no alkali addition, KCl only and NaCl only. The KCl and NaCl samples both exhibit efficiency close to 10% and comparable PV parameters.

Sample	Eff. (%)	FF (%)	V _{OC} (mV)	J _{SC} (mAcm ⁻²)	A	J ₀ (mAcm ⁻²)	E _g -qV _{OC} (eV)	N _C (cm ⁻³)
No alkali addition	6.4	51.6	364	33.8	1.21	4.3E-04	0.63	6.6E15
10 mM KCl	9.7	61.0	432	36.7	1.24	7.0E-5	0.59	1.6E16
100 mM NaCl	10.1	65.0	428	36.5	1.27	1.3E-04	0.57	2.2E16

A shift to higher bandgaps of up to 1.04 eV can also be observed, similar to the sample series only containing KCl.

Finally, Table II presents a comparison of the best cells obtained from nominally alkali-free, KCl- and NaCl-containing absorbers. The addition of either alkali element can yield high-efficiency devices around 10 % with comparable photovoltaic properties. However, a ten-fold lower concentration of potassium is sufficient for achieving similar efficiencies to the sodium-containing sample.

IV. CONCLUSIONS

It has been confirmed that the addition of potassium into the kesterite absorber layer leads to an enhanced grain growth and improved PV properties, however the potassium-containing devices do not outperform sodium-containing counterparts. Compared to sodium, a ten-fold lower potassium amount is sufficient to achieve similar grain size and device performance. The reduction of series resistance of solar cells previously reported is confirmed by this study. Potassium doping increases the carrier concentration as derived from C-V measurements. Higher nominal Potassium concentrations require an adjustment of the tin content in the absorber layer in order to avoid formation of Sn(S,Se)₂ secondary phase and thus deterioration of the device performance. Synergetic effects between potassium and sodium are not observed and both alkali elements exhibit similar beneficial effects on the kesterite solar cell performance.

SUPPLEMENTARY MATERIAL

See [supplementary material](#) for the SIMS image of the inhomogeneous potassium distribution inside the absorber layer and the detailed measurements of the 400/008 Bragg reflexes of the KCl only and NaCl + KCl samples and.

ACKNOWLEDGMENTS

This research was supported by the Framework 7 program under the project KESTCELLS (FP7-PEOPLE-2012-ITN-316488) and by the Horizon 2020 program under the project STARCELLS (H2020-NMBP-03-2016-720907). C.A. acknowledges support from the Swiss National Science Foundation, project IZLIZ2_157140/1. The authors would also like to thank the whole team of the Laboratory for Thin Films and Photovoltaics.

¹ W. Wang, M. T. Winkler, O. Gunawan, T. Gokmen, T. K. Todorov, Y. Zhu, and D. B. Mitzi, *Adv. Energy Mater.* **4**, 1700167 (2014).

² C. M. Sutter-Fella, J. A. Stückelberger, H. Hagendorfer, F. La Mattina, L. Kranz, S. Nishiwaki, A. R. Uhl, Y. E. Romanyuk, and A. N. Tiwari, *Chem. Mater.* **26**, 1420 (2014).

³ T. Gershon, B. Shin, N. Bojarczuk, M. Hopstaken, D. B. Mitzi, and S. Guha, *Adv. Energy Mater.* **5**, 1400849 (2015).

⁴ X. Liu, Y. Feng, H. Cui, F. Liu, X. Hao, G. Conibeer, D. B. Mitzi, and M. Green, *Prog. Photovolt: Res. Appl.* **24**, 879 (2016).

⁵ A. Chirilă, P. Reinhard, F. Pianezzi, P. Bloesch, A. R. Uhl, C. Fella, L. Kranz, D. Keller, C. Gretener, H. Hagendorfer, D. Jaeger, R. Erni, S. Nishiwaki, S. Buecheler, and A. N. Tiwari, *Nat. Mater.* **12**, 1107 (2013).

⁶ S. G. Haass, M. Diethelm, C. Andres, Y. E. Romanyuk, and A. N. Tiwari, *Thin Solid Films* **633**, 131 (2017).

⁷ E. Ghorbani, J. Kiss, H. Mirhosseini, T. D. Kühne, and C. Felser, in *2015 IEEE 42nd Photovoltaic Specialist Conference (PVSC)*, pp. 1–3 (2015).

⁸ T. Maeda, A. Kawabata, and T. Wada, *Phys. Status Solidi C* **12**, 631 (2015).

⁹ W. Li, Z. Su, J. M. R. Tan, S. Y. Chiam, H. L. Seng, S. Magdassi, and L. H. Wong, *Chem. Mater.* **29**, 4273 (2017).

¹⁰ T. Schwarz, O. Cojocar-Mirédin, P. Choi, M. Mousel, A. Redinger, S. Siebentritt, and D. Raabe, *JAP* **118**, 095302 (2015).

- ¹¹ M. Johnson, S. V. Baryshev, E. Thimsen, M. Manno, X. Zhang, I. V. Veryovkin, C. Leighton, and E. S. Aydil, [Energy Environ. Sci.](#) **7**, 1931 (2014).
- ¹² Z. Tong, C. Yan, Z. Su, F. Zeng, J. Yang, Y. Li, L. Jiang, Y. Lai, and F. Liu, [Applied Physics Letters](#) **105**, 223903 (2014).
- ¹³ Y.-T. Hsieh, Q. Han, C. Jiang, T.-B. Song, H. Chen, L. Meng, H. Zhou, and Y. Yang, [Adv. Energy Mater.](#) **6**, 1502386 (2016).
- ¹⁴ T. Abzieher, T. Schnabel, M. Hetterich, M. Powalla, and E. Ahlswede, *Phys. Status Solidi A* **4**, 1039 (2015).
- ¹⁵ C. M. Sutter-Fella, J. A. Stückelberger, H. Hagendorfer, F. La Mattina, L. Kranz, S. Nishiwaki, A. R. Uhl, Y. E. Romanyuk, and A. N. Tiwari, [Chem. Mater.](#) **26**, 1420 (2014).
- ¹⁶ J. Sangster and A. D. Pelton, *Journal of Phase Equilibria* **18**, 177 (1997).
- ¹⁷ P. Reinhard, B. Bissig, F. Pianezzi, E. Avancini, H. Hagendorfer, D. Keller, P. Fuchs, M. Döbeli, C. Vigo, P. Crivelli, S. Nishiwaki, S. Buecheler, and A. N. Tiwari, [Chem. Mater.](#) **27**, 5755 (2015).
- ¹⁸ O. Cojocaru-Mirédin, P. Choi, D. Abou-Ras, S. Schmidt, R. Caballero, and D. Raabe, *IEEE Journal of Photovoltaics* **1**(2), 207 (2011).
- ¹⁹ K. Liu, H. Liu, J. Wang, and L. Feng, *Materials Letters* **63**, 512 (2009).
- ²⁰ M. Paris, G. Larramona, P. Bais, S. Bourdais, A. Lafond, C. Choné, C. Guillot-Deudon, B. Delatouche, C. Moisan, and G. Dennler, *J. Phys. Chem. C* **119**, 26849 (2015).
- ²¹ S. G. Haass, C. Andres, R. Figi, C. Schreiner, M. Bürki, Y. E. Romanyuk, and A. N. Tiwari, *Advanced Energy Materials* (2017).
- ²² M. Burgelman, J. Verschraegen, S. Degraeve, and P. Nollet, *Prog. Photovolt: Res. Appl.* **12**, 143 (2004).
- ²³ D. Cozza, Ph.D. thesis, Aix-Marseille Université, Aix-Marseille (France), 2016.
- ²⁴ S. G. Haass, M. Diethelm, M. Werner, B. Bissig, Y. E. Romanyuk, and A. N. Tiwari, [Adv. Energy Mater.](#) **5**, 1500712 (2015).
- ²⁵ J. Sangster and A. D. Pelton, *Journal of Phase Equilibria* **18**, 185 (1997).